

We are IntechOpen, the world's leading publisher of Open Access books Built by scientists, for scientists

6,900

Open access books available

186,000

International authors and editors

200M

Downloads

Our authors are among the

154

Countries delivered to

TOP 1%

most cited scientists

12.2%

Contributors from top 500 universities



WEB OF SCIENCE™

Selection of our books indexed in the Book Citation Index
in Web of Science™ Core Collection (BKCI)

Interested in publishing with us?
Contact book.department@intechopen.com

Numbers displayed above are based on latest data collected.
For more information visit www.intechopen.com



Terahertz Leaky-Wave Antennas Based on Metasurfaces and Tunable Materials

Walter Fuscaldo, Silvia Tofani, Paolo Burghignoli,
Paolo Baccarelli and Alessandro Galli

Additional information is available at the end of the chapter

<http://dx.doi.org/10.5772/intechopen.78939>

Abstract

Terahertz frequencies are increasingly gaining attention due to the recent efforts made in narrowing the technological gap among microwave and optical components. Still the demand of efficient THz antennas is high, due to the difficulty in obtaining directive patterns and good radiation efficiencies with planar, low-cost, easy-to-fabricate designs. In this regard, leaky-wave antennas have recently been investigated in the THz range, showing very interesting radiating features. Specifically, the combination of the leaky-wave antenna design with the use of metamaterials and metasurfaces seems to offer a promising platform for the development of future THz antenna technologies. In this Chapter, we focus on three different classes of leaky-wave antennas, based on either metasurfaces or tunable materials, namely graphene and nematic liquid crystals. While THz leaky-wave antennas based on homogenized metasurfaces are shown to be able to produce directive patterns with particularly good efficiencies, those based on graphene or nematic liquid crystals are shown to be able to dynamically reconfigure their radiating features. The latter property, although being extremely interesting, is obtained at the expense of an increase of costs and fabrication complexity, as it will emerge from the results of the presented study.

Keywords: terahertz, leaky-wave antennas, metasurfaces, graphene, liquid crystals

1. Introduction

Metamaterials and metasurfaces [1] are, respectively, three-dimensional (3-D) and two-dimensional (2-D) engineered man-made materials, which may exhibit electromagnetic properties commonly unaccessible with materials available in nature. Since the introduction of

Transformation Optics in 2006 by Pendry [2], metasurfaces have represented a privileged platform for achieving a considerable control of electromagnetic waves propagation. *Electromagnetic cloaking* and *metasurfing*, i.e., controlling surface or guided waves through tunable metasurfaces [3], are one of the most known applications of metasurfaces. However, in this Chapter, we focus on the application of metasurfaces for the realization of *reconfigurable leaky-wave antennas* (LWAs) [4].

In the microwave range, there exists numerous realizations of metasurfaces (see, e.g., [4] and refs. therein), but at terahertz (THz) frequencies (nominally comprised between 300 GHz and 3 THz [5]), very few designs are available. Nowadays, THz technology is recognized as one of the most promising and challenging area of research for a twofold reason: (i) on the one hand, the wide and interdisciplinary character of THz applications, spanning from molecular spectroscopy and astrophysics, to high data rate communications and high-resolution imaging, passing through security screening and drug detection [6]; (ii) on the other hand, the increasing availability of efficient THz sensors and sources [7] that have recently contributed to considerably narrow the so-called *THz gap*.

Nevertheless, the demand of efficient THz antennas is still high [6]. Indeed, even though various solutions have been proposed (see, e.g., [8–11]), efficient realizations often require high fabrication costs and complexity [11]. To better handle the efficiency vs. cost/complexity tradeoff, *leaky-wave antennas* [12] have been proposed and experimentally demonstrated as valid alternatives for the design of efficient, low-cost, THz antennas [13, 14]. Such prototypes [13, 14] present many advantages with respect to previous THz antenna solutions, but their lens-like structure does not allow for a planar design, an attractive feature for micromachined packaging of THz systems [11]. In this regard, more recently, a specific class of LWAs based on Fabry-Perot cavities (FPCs), i.e., FPC-LWAs, has been proposed as low-profile, fully-planar, directive, and efficient THz antennas [15]. Even more interestingly, tunable materials such as *graphene* [16] and *liquid crystals* [17] have recently been employed for the realization of FPC-LWAs showing beam-steering capabilities at fixed frequency [18–22].

This Chapter is devoted to the analysis and design of novel THz FPC-LWAs. In Section 2, the general properties and the radiating features of FPC-LWAs are briefly reviewed. Conventional and more advanced designs are presented, with a specific focus on the technological constraints that typically affect the design of FPC-LWAs in the THz range. In Section 3, the design of THz FPC-LWA based on a homogenized metasurface is presented. The choice of a fishnet-like unit-cell is motivated by its remarkably low spatial dispersion and the capability of achieving a high reflectivity with a feasible variation of its structural parameters. The THz FPC-LWA considered in Section 3 produces a considerably high gain, but it does not allow for pattern reconfigurability. In Sections 4 and 5, two reconfigurable THz FPC-LWAs are therefore presented. In Section 4, the capabilities of two different THz FPC-LWAs based on graphene are shown and compared. The tunability of the graphene impedance through a DC voltage allows for a wide reconfigurability of the pattern. In Section 5, nematic liquid crystals are employed as tunable materials in a THz FPC-LWA to enhance the control of the beam angle through the application of a low-driving voltage. Finally, conclusions are drawn in Section 6.

2. Fabry-Perot cavity leaky-wave antennas (FPC-LWAs)

Fabry-Perot cavity leaky-wave antennas (FPC-LWAs) are partially open waveguiding structures, which support *cylindrical leaky waves* that radially propagate outward from the source [12, 23]. In this class of structures, radiation occurs through the excitation of the fundamental leaky modes supported by the structure, which are forward fast waves. Interestingly, when the excitation is a horizontal dipole (either electric or magnetic), the fundamental pair of TE, TM leaky modes is excited, and an FPC-LWA may produce a directive pencil beam at broadside or a conical beam with the cone axis along the vertical x -axis (see **Figure 1**) [12, 23, 24].

The architecture of an FPC-LWA relies on a grounded dielectric slab (GDS) covered with a partially reflecting screen (PRS) [25]. The gain enhancement phenomenon of these structures was originally explained through a ray-optics interpretation based on the Fabry-Perot concept [25] in the 1950s. However, the radiating features of these structures are more conveniently explained under the frame of the leaky-wave theory [12]. Indeed, due to the generality of the leaky-wave interpretation, the PRS can take various forms (e.g., a homogenized metasurface [24, 26] as in **Figure 1(a)**, a denser dielectric superstrate [27, 28] as in **Figure 1(b)**, and a distributed Bragg reflector [29] as in **Figure 1(c)**) provided that is suitably modeled with homogenized effective materials (when the PRS is *bulky*, e.g., a *metamaterial*) or surface impedances (when the PRS is *planar*, e.g., a *metasurface*). Regardless of the type of PRS, the leaky-wave approach yields to the same design process. This has allowed for the introduction of a variety of FPC-LWA designs, especially in the microwave range.

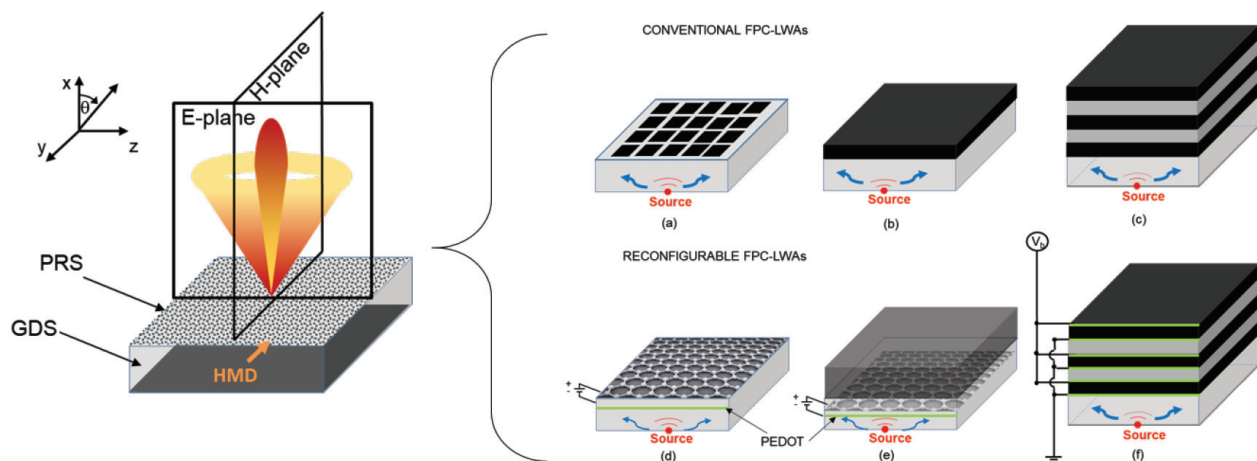


Figure 1. On the left, a typical FPC-LWA example fed by a horizontal magnetic dipole oriented along the y -axis. Depending on the operating point, such an antenna is able to produce either a pencil beam at broadside, or a conical beam. (a)–(f) Illustrative examples of Fabry-Perot cavity leaky-wave antennas (FPC-LWAs). (a)–(c) Conventional FPC-LWAs based on (a) a homogenized metasurface, (b) a high-permittivity dielectric cover layer (substrate-superstrate design), and (c) a distributed Bragg reflector (multiple layers dielectric structure). (d)–(f) Reconfigurable FPC-LWAs based on (a) a tunable graphene sheet, (b) a tunable graphene sheet in a substrate-superstrate configuration, and (c) a distributed Bragg reflector made of tunable nematic liquid crystals cells.

2.1. Radiating properties of 2-D LWAs

The radiating features of an FPC-LWA qualitatively depend on the type of excitation that is considered [23]. In this Chapter, the FPC-LWAs under investigation are always assumed to be fed by horizontal magnetic dipoles (HMDs). This choice is motivated by (i) the constraints dictated by THz technology, as will appear more clearly in Section 2.6; and (ii) the interest in achieving broadside radiation, a feature that is never possible with vertical dipoles [23].

As it has been rigorously shown in [23], an HMD source launches a pair of leaky waves, one TM and one TE, both characterized by a (complex) leaky wavenumber $k_z = \beta_z - j\alpha_z$ ¹, where β_z and α_z are the phase and attenuation constants, respectively. Under certain conditions [30, 31] (usually met by a properly designed FPC-LWA [26]), the fundamental TE, TM pair of leaky modes is sufficient to describe radiation from such FPC-LWAs. In this case, the TM leaky wave determines the E-plane pattern, while the TE leaky wave determines the H-plane pattern [23]. For a broadside beam, these two leaky waves have very nearly the same phase and attenuation constants, and hence an omnidirectional *pencil* beam is created. Its beamwidths $\Delta\theta$ on the E- and H-planes are given by:

$$\Delta\theta_E = 2\sqrt{2}\hat{\alpha}_z^{\text{TM}}, \quad \Delta\theta_H = 2\sqrt{2}\hat{\alpha}_z^{\text{TE}}, \quad (1)$$

where the $\hat{(\cdot)}$ identifies normalization to the vacuum wavenumber k_0 (i.e., $\hat{k}_z = k_z/k_0 = \hat{\beta}_z - j\hat{\alpha}_z$), whereas the superscripts TE(TM) refers to the corresponding polarization.

For scanned beam $\beta_z \gg \alpha_z$, the beamwidths are given by [23]:

$$\Delta\theta_E = 2\hat{\alpha}_z^{\text{TM}} \sec \theta_0^{\text{TM}}, \quad \Delta\theta_H = 2\hat{\alpha}_z^{\text{TE}} \sec \theta_0^{\text{TE}}, \quad (2)$$

where $\theta_0^{\text{TE}}(\theta_0^{\text{TM}})$ is the pointing angle (measured from the vertical x -axis) with respect to the H(E)-plane, whose expression reads [26]

$$\sin \theta_0 = \sqrt{\hat{\beta}_z^2 - \hat{\alpha}_z^2}. \quad (3)$$

Equation (3) clearly defines the different radiating regimes of an FPC-LWA: when $\beta_z < \alpha_z$, the antenna radiates at broadside, otherwise it radiates a scanned beam. At the limiting condition, i.e., when $\beta_z = \alpha_z$, also known as *leaky cutoff condition* or *splitting point*, the antenna radiates the maximum power density at broadside.

From Eqs. (1)–(3) it is clear that, as the wavenumbers of the two leaky waves begin to differ, the beamwidths and the pointing angles become different on the principal planes. This typically happens as the scan angle increases. Consequently, a desirable property for a PRS is to show almost the same behavior for both the TM and the TE polarization, especially when the angle of incidence changes. In fact, this would allow for having the equalization of the TM, TE leaky wavenumbers, which in turn produces nearly circular conical scanned beams [32].

¹For the sake of simplicity, the z -axis is here chosen as the preferred axis of propagation.

2.2. Design rules for FPC-LWAs

In all PRS-based FPC-LWAs, the PRS is used to create a leaky parallel plate waveguide (PPW) region, and the leaky waves are leaky (radiating) versions of the PPW guided modes that would be excited by the source in an ideal PPW, which results if the PRS is replaced by a perfect electric conductor (PEC) wall. This point of view allows for a simple design formula for the thickness of the dielectric layer in order to obtain a beam at a desired angle θ_0 (either a broadside or a conical beam).

For m -th order TM and TE PPW modes, the radial wavenumber of an ideal PPW would be $\beta_z = \beta_z^{\text{TM}} = \beta_z^{\text{TE}} = \sqrt{k_0^2 \epsilon_r - (m\pi/h)^2}$, where h is the thickness of the dielectric substrate and ϵ_r its relative permittivity. Using Eq. (3) (under the assumption that $\hat{\beta}_z \gg \hat{\alpha}_z$), one finds the following design rule

$$h = m\lambda_0/2(\epsilon_r - \sin^2\theta_0)^{-1/2}. \quad (4)$$

Typically, FPC-LWAs operate with the fundamental (i.e., $m = 1$) leaky mode pair under the condition of broadside radiation (i.e., $\theta_0 = 0^\circ$); thus, the design rule reduces to $h = 0.5\lambda_0/\sqrt{\epsilon_r}$.

It should be mentioned that the previous equations are found under the hypothesis that the FPC-LWA is of infinite transverse extent. This assumption holds as long as the leaky mode radiates most of its power as it approaches the lateral truncation. By defining the radiation efficiency η_r as the ratio between the radiated power P_{rad} and the initial power P_{in} , it results $\eta_r := P_{\text{rad}}/P_{\text{in}} = 1 - e^{-\alpha_z L}$ (L being the transverse size of the cavity), and hence,

$$L/\lambda_0 = -\ln(1 - \eta_r)/(2\pi\hat{\alpha}_z). \quad (5)$$

This furnishes a design rule for the lateral truncation. Usually the antenna size is designed so that the FPC-LWA reaches at least a radiation efficiency $\eta_r = 90\%$, and thus Eq. (5) reduces to $L/\lambda_0 = 0.366/\hat{\alpha}_z$. However, this design rule assumes the structure to be lossless. When losses are present, the efficiency of the structure should be scaled of a factor $\hat{\alpha}_{\text{rad}}/\hat{\alpha}_z$ [33], where $\hat{\alpha}_{\text{rad}}$ is the leakage rate produced by the ideal lossless structure. The efficiency in a lossless structure is therefore given by $\eta_r \alpha_{\text{rad}}/\alpha_z$.

Finally, the optimal location of the source depends on its polarization. An HMD source maximizes the peak power density when it is placed on the ground plane [12]. However, the source location usually has little effect on the pattern shape, since this is dictated by the leaky-wave phase and attenuation constants. In particular, the phase constant is primarily determined by the thickness of the dielectric layer, while the attenuation constant is primarily determined by the properties of the PRS.

2.3. Circuit model for FPC-LWAs

Regardless of the type of PRS, it is convenient to characterize its electromagnetic behavior in terms of a PRS impedance (admittance) Z_{PRS} ($Y_{\text{PRS}} = 1/Z_{\text{PRS}}$). Under these assumptions,

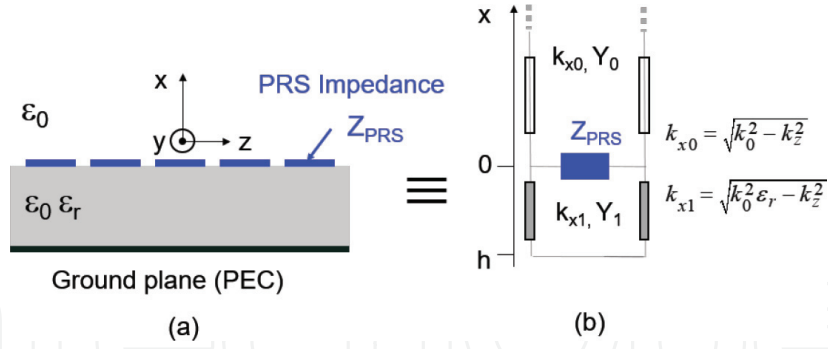


Figure 2. (a) 2-D section of an FPC-LWA and (b) its equivalent circuit model.

FPC-LWAs are conveniently studied with an equivalent circuit model. Once Z_{PRS} is known, the transverse resonance technique [12] can be applied to the equivalent circuit model (see **Figure 2**) to derive the relevant dispersion equations for the TE and TM modes

$$Y_0^p + Y_{\text{PRS}}^p - jY_1^p \cot(k_0 h \hat{k}_{x1}) = 0, \quad (6)$$

where the equivalent admittances in air Y_0^p and inside the slab Y_1^p , $p \in \{\text{TE}, \text{TM}\}$ for TE and TM modes have the following expressions:

$$Y_0^{\text{TM}} = \varepsilon_r / (\hat{k}_{x0} \eta_0), \quad Y_1^{\text{TM}} = 1 / (\hat{k}_{x1} \eta_0), \quad Y_0^{\text{TE}} = \hat{k}_{x0} / \eta_0, \quad Y_1^{\text{TE}} = \hat{k}_{x1} / \eta_0, \quad (7)$$

where $\eta_0 \simeq 120\pi\Omega$ is the vacuum impedance, whereas $\hat{k}_{x0} = \sqrt{1 - \hat{k}_z^2}$ and $\hat{k}_{x1} = \sqrt{\varepsilon_r - \hat{k}_z^2}$ are the normalized vertical wavenumbers in air and in the dielectric, respectively. The zeros of Eq. (6) represent the wavenumbers of the eigenmodes of the structure in both the bound $\hat{\beta}_z > 1$ (i.e., surface waves) and the radiative $\hat{\beta}_z < 1$ (i.e., fast leaky waves) regimes².

In the case of a substrate-superstrate, or multiple-layer configurations (see **Figures 1(a)** and **(b)**), the layers can be treated as transmission line segments, and the resulting PRS impedance can be modeled as the input impedance seen looking upward from the substrate interface. Such an input impedance will take two different expressions depending on whether the TM or the TE polarization is considered. The previous dispersion equations will thus hold, provided that the correct input admittances are substituted to Y_{PRS}^p .

In the case of homogenized metasurfaces, the concept of surface impedance is conveniently introduced (see [26, 34]). While in general the surface impedance is described by a tensorial surface impedance $\underline{\underline{Z}}_s$ (see [35] for further details), throughout the Chapter, we will always

²It is worth recalling that surface waves are *proper* waves (*improper* surface waves exist from a mere mathematical point of view, but they are not physically meaningful) since they exponentially decay in the vertical direction $\alpha_x > 0$, whereas forward ($\hat{\beta}_z > 0$) leaky waves are *improper* waves, as they exponentially grow in the vertical direction $\alpha_x < 0$. This does not compromise the physical significance of leaky waves, since the exponentially-growing character of leaky waves is maintained only within a limited angular region, and thus they do not violate the Sommerfeld radiation condition at infinity (see [30, 31] for a rigorous discussion).

deal with materials which allow for describing the PRS impedance with a scalar value: more precisely, one for the TE polarization and one for the TM polarization. Indeed, we will always assume a negligible TE-TM cross coupling, thus reducing the dyadic surface impedance to a diagonal matrix. The previous dispersion equations will thus hold, provided that the correct surface admittances are substituted to Y_{PRS}^p .

2.4. Conventional FPC-LWAs

As manifested from Eqs. (1)–(3), the beamwidths and the beam angles depend on the leaky wavenumber [12, 36, 37]. As the leaky wavenumber of an FPC-LWA depends on frequency (as a solution of the dispersion Eq. (6)), the radiating properties of a conventional FPC-LWA also depend on frequency. Indeed, the frequency scanning behavior is a distinctive feature common to all LWAs (not only FPC-type LWAs) [12]. All the structures outlined in this Section 2.4 are therefore referred to as *conventional* FPC-LWAs in the sense that they do not employ any technique to avoid their intrinsic frequency scanning behavior.

2.4.1. Homogenized metasurfaces

A homogenized metasurface (HMS) is characterized by a periodic lattice of “subresonant” elements, i.e., with period $p \ll \lambda_0$. Note that throughout the Chapter, we assume to deal with a patterned metallic screen, treating the metal as a PEC. This is still a good approximation at THz frequencies, provided that one considers thick enough (thicker than the skin depth [38]) good metals such as copper, aluminum, silver, and gold.

The hypothesis $p \ll \lambda_0$ is also known as the *homogenization limit* [34] and, as long as it is fulfilled, it allows for describing the electromagnetic behavior of the surface impedance through the generalized sheet transition conditions (GSTCs) [35]. Under this formalism, the tensorial surface impedance $\underline{\underline{Z}}_s$ is usually expressed as a diagonal matrix (no TE-TM coupling is assumed) whose diagonal elements $Z_s^{\text{TE}}, Z_s^{\text{TM}}$ are modeled with a purely imaginary impedance $Z_s = jX_s$ (no ohmic losses are expected for HMSs made by PEC), X_s being the surface reactance. Furthermore, when dealing with HMS-based FPC-LWAs radiating at *broadside*, there is no distinction between the diagonal elements, and thus $Z_s^{\text{TM}} = Z_s^{\text{TE}} = jX_s$.

Interestingly, as long as $X_s \ll \eta_0$, it has been shown [26] that the directivity at *broadside* D_0 is inversely proportional to the square of X_s , whereas the fractional bandwidth FBW (defined as the range of frequency, normalized to the operating frequency, for which the radiated power density at broadside decreases by less than 3 dB) is directly proportional to the square of X_s ³

$$D_0 \simeq \frac{\pi^2}{2\sqrt{\epsilon_r^3}} \frac{\eta_0^2}{X_s^2}, \quad \text{FBW} = \frac{2\sqrt{\epsilon_r} X_s^2}{\pi \eta_0^2} + \tan \delta, \quad (8)$$

where $\tan \delta$ is the loss tangent of the dielectric filling (which is nonnegligible in the THz range).

³We note here that in the expression of D_0 published in [15] a factor $0.5/\epsilon_r$ was missing, and is now correctly included in Eq. (8).

As manifested in Eq. (8), a tradeoff is established between FBW and D_0 . Consequently, lower values of X_s lead to highly directive FPC-LWAs working in a narrow bandwidth, whereas higher values of X_s lead to moderately-directive FPC-LWAs working in a considerable bandwidth. To give some numbers, directivities higher than 30 dB can be obtained with $X_s < 20 \Omega$, assuming $\varepsilon_r = 2.3$.

The previous relations hold for broadside radiation. When the antenna radiates a scanned beam, the TM and the TE surface impedances of an HMS generally differ each other. Indeed, the dependence of the surface impedance on the angle of incidence (spatial dispersion) and frequency (temporal dispersion) should be taken into account in a thorough characterization of an HMS. A canonical example is that of patch array and its complementary structure (according to Babinet's principle), the strip grating (see **Figure 3(a)**). Indeed, the grid impedance of an array of patches (a strip grating) for TE(TM) polarization exhibits a spatially dispersive character because it depends on the angle of incidence θ . The formula for the HMS of a strip grating and a patch array of infinite extent are given in [34], and are here applied for obtaining results in **Figures 3(b)** and **(c)**, assuming a lattice of period $p = \lambda/10$ with $w = p/10$ and $g = p/10$ for the strips and the patches, respectively. As is manifest from **Figures 3(b)** and **(c)** the presented topologies (strip and patch) allow for synthesizing low impedances only for unfeasible values of their structural parameters (i.e., g and w) in the THz range. For example, at 1 THz and for $\theta = 0^\circ$, an impedance of 20Ω is reached with a strip grating with strips narrower than $3 \mu\text{m}$. As it will appear clearly in Section 2.6, this value could present some issues during the photolithography fabrication process [15]. Moreover, the high variation of the reactance with respect to the angle of incidence would produce very different radiating features as the beam is scanned from broadside to endfire.

However, several HMS geometries with limited spatial dispersion for both TE and TM polarizations have been proposed in the literature [35, 39], even for the development of highly directive FPC-LWAs [15]. Among them, the so-called fishnet geometry (see **Figure 3(a)**), i.e., a superposition between the patch and the strip layouts, will be investigated in Section 3. We note that the synthesis of HMSs with limited spatial dispersion is a key aspect for the development of reconfigurable LWAs. In fact, it allows for designing and optimizing the radiating properties of a reconfigurable FPC-LWA at broadside (i.e., $\theta = 0^\circ$), without affecting the impedance properties as the beam is steered.

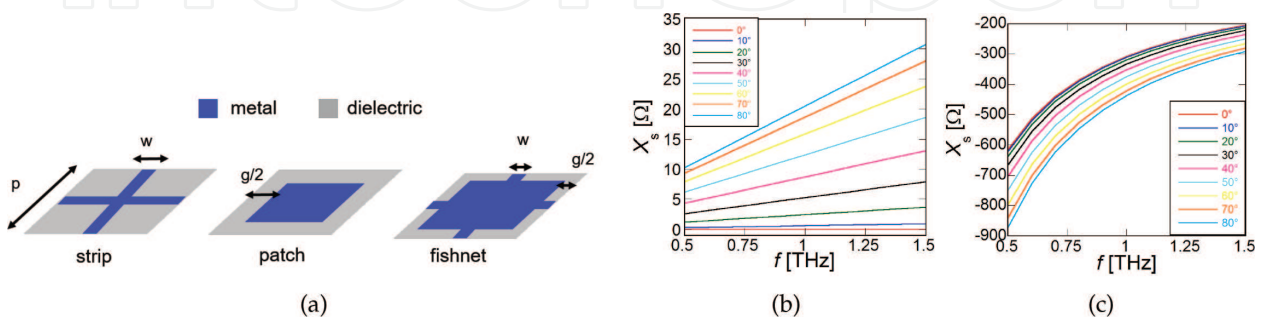


Figure 3. (a) Unit cells of three different type of HMSs: the strip grating, the array of patches, and the fishnet. (b) and (c) Surface reactance X_s vs. frequency in the range $0.5 < f < 1.5$ [THz] for angles of incidence in the range $0^\circ \leq \theta \leq 80^\circ$ with angular steps of 10° : (b) strip grating for TM polarization and (c) array of patches for TE polarization (parameters in the text).

2.4.2. Substrate-superstrate structure

In a substrate-superstrate configuration, the PRS is represented by a cover layer made of a denser dielectric material with respect to the substrate, as depicted in **Figure 1(b)**. These kinds of structures, commonly known as *substrate-superstrate* (SS) LWAs, have been extensively studied by N. G. Alexópoulos and D. R. Jackson [27, 40]. In those works [27, 40], they showed that the PRS (represented by the superstrate) would act as an almost perfectly reflecting layer, when the thickness h_2 of the superstrate (the *cover* layer) is chosen so that it is an odd multiple of one-quarter of the wavelength in the vertical direction. This corresponds to the condition

$$h_2 = (2m - 1)\lambda/4(\epsilon_{r2} - \sin^2\theta_0)^{-1/2}. \quad (9)$$

It is clear from Eqs. (4) and (9) that the design rules for optimizing radiation at broadside ($\theta_0 = 0$) with the fundamental ($m = 1$) TE, TM leaky modes suggest a thickness of a half- and of a quarter-wavelength in their respective media for the substrate and the superstrate, respectively.

Another distinctive feature of SS-LWAs is that the directivity increases as the permittivity of the superstrate layer increases with respect to that of the substrate layer since the superstrate PRS acts as a more reflective surface.

2.4.3. Multilayered dielectric structure

As shown in [27, 28], a very high step index (i.e., $\sqrt{\epsilon_{r2}/\epsilon_r}$) is required for achieving relatively high directivities with a substrate-superstrate configurations. As high-permittivity materials usually exhibit also nonnegligible loss tangent, the radiation efficiency of a substrate-superstrate FPC-LWA is often limited by the relatively high dielectric losses of the dielectric layers. In this regard, a different way to increase directivity was proposed in [41]. There, the single superstrate is replaced by a periodic array of such superstrates, as shown in **Figure 1(c)**. In this structure, the PRS consists of a stack of multiple alternating layers of high permittivity and low permittivity, whose thicknesses are chosen according to Eq. (9). As shown in [41], the directivity increases geometrically with the number of superstrate layers, and thus very directive beams may be obtained using modest values of superstrate permittivity, provided that several superstrate layers are used. From a circuital point of view, the gain enhancement phenomenon of this class of structures is readily explained by noticing that the $2n - 1$ quarter-wavelength sections reduce the free-space impedance (seen as a load impedance of the transmission line segment looking upward from the substrate interface) of a factor $(\epsilon_{r2}/\epsilon_r)^n$.

As a last remark, it is worth noting that the multistack of alternating layers can be interpreted as a *distributed Bragg reflector* (DBR) meaning that it is a periodic *electromagnetic bandgap* (EBG) structure operating in a stopband. From this point of view, the substrate acts as a defect in the periodic EBG structure [42]. More interestingly, a leaky-wave explanation of the phenomenon is provided in [29].

2.5. Reconfigurable FPC-LWAs

In most of microwave applications, the frequency scanning behavior typical of conventional FPC-LWAs is an undesirable effect, since the antenna radiating performance should not change within a small fractional bandwidth centered around the operating frequency. Conversely, it

would be extremely beneficial, e.g., for *SATCOM applications* to dynamically change certain radiating properties (e.g., the pointing angle) at a fixed frequency. This would allow for avoiding solutions based on either heavy mechanical rotation systems or expensive 2-D phased arrays.

The idea at the root of a reconfigurable FPC-LWA is instead simple and effective. In order to obtain the beam-steering capability in an FPC-LWA, it is necessary to change the phase constant of the relevant leaky mode excited in the cavity at a fixed frequency. This can be done, e.g., by dynamically changing the relevant geometrical or electromagnetic parameters of the materials, i.e., the thicknesses of the layers, or the relative permittivities and permeabilities (surface impedances for zero-thickness layers), respectively. While this possibility has extensively been addressed in the microwave range through, e.g., active impedances [43], or ferroelectric and ferromagnetic materials [44], few realizations exist in the THz range [20, 22, 45, 46].

In those works [20, 22, 45, 46], a tunable metasurface (e.g., graphene [20, 45, 46]) or a tunable material (e.g., nematic liquid crystals [22]) are employed as shown in **Figures 1(d)–(f)**, respectively. The idea is to exploit the voltage dependence of either the surface conductivity of graphene (*ambipolar field effect* [47]) or the dielectric permittivity of a nematic liquid crystal (*nematic phase transition* [17]). Therefore, by changing the electromagnetic properties of the material, one can affect the leaky wavenumber (and, in turn, the radiating beam properties of an FPC-LWA) by applying a control voltage through a biasing scheme. The realization of such biasing schemes in the THz range is challenging and thus motivates the lack of reconfigurable THz FPC-LWA realizations. This and other aspects concerning the severe constraints posed by THz technology are discussed in the next Section 2.6.

2.6. FPC-LWAs in the THz range

When a reconfigurable FPC-LWA has to be designed in the THz range, one has to consider several additional technological constraints: (i) the availability of low loss THz materials, (ii) the availability of efficient THz sources, (iii) the fabrication tolerances, and (iv) the complexity in the realization of a biasing scheme. These aspects are discussed below on a point-by-point basis.

2.6.1. THz materials

An FPC-LWA consists of a grounded dielectric substrate of thickness $0.5\lambda/\sqrt{\epsilon_r}$ covered with a PRS. In order to limit the losses in the cavity, the dielectric material should preferably exhibit a low loss tangent in the THz range. Examples of such materials are Zeonor ($\epsilon_r = 2.3$ and $\tan \delta = 0.001$) and quartz ($\epsilon_r = 3.8$ and $\tan \delta = 0.014$). The latter, even if characterized by a loss tangent greater by an order of magnitude with respect to that of Zeonor, is particularly amenable for the realization of graphene-based structures. Indeed, graphene, when transferred on SiO_2 , shows limited phonon scattering [48], an effect that heavily contributes to decreasing the quality of graphene during its synthesis (see [49] for further details).

2.6.2. THz sources

The FPC-LWAs investigated here are assumed to be excited with an HMD. This type of excitation can be realized by etching a subresonant slot in the ground plane. Such a slot can be either back-illuminated with a coherent THz source, or fed with a THz waveguide. These

two types of excitations suggest to realize a quasi-resonant slot (thus modeling a half-wavelength dipole rather than a short dipole) for a twofold reason. With regard to free-space excitation, one has to consider that commercially available THz lenses focus on the energy over a spot size around 1 mm with a 2-D Gaussian profile [50]. As a result, a good energy coupling is obtained if one considers a slot of dimensions not less than $100 \mu\text{m}$; such a dimension corresponds to $\lambda/3$ at the targeted frequency of 1 THz. With regard to guided wave excitation, one has to consider the cross section of commercial THz waveguides operating in the THz range. In the 900–1400 GHz band, the waveguide cross section is $200 \mu\text{m} \times 100 \mu\text{m}$ [15], corresponding to $2\lambda/3 \times \lambda/3$ at 1 THz.

2.6.3. THz fabrication tolerance

In Section 2.4, we have seen that the PRS of an FPC-LWA may consist of a homogenized metasurface (HMS). As an HMS consists of a periodic lattice of subresonant elements, patterning of these elements on a metallic sheet is subject to the fabrication tolerances. Since the smallest details commonly allowed in a standard photolithographic process should be greater than $3 \mu\text{m}$ to avoid fabrication issues in low-cost, large-area production [15], the unit-cell period is set to $p = \lambda_0/5 = 60 \mu\text{m}$. On the one hand, this value fulfills the homogenization limit [34] (p should preferably be smaller than $\lambda_0/4$). On the other hand, the choice of $p = \lambda_0/5$ allows for designing details of the mask down to $p/20$ when designing the HMS at 1 THz.

2.6.4. THz biasing scheme

The realization of a biasing scheme in a reconfigurable THz FPC-LWA based on graphene differs from that of an FPC-LWA based on nematic liquid crystals (NLCs). In an NLC-based FPC-LWA, a pair of conductive layers “sandwich” the NLC cell. However, a conductive layer introduces ohmic losses in the cavity; hence, it is important to use quasi-transparent polymers in the THz range. We therefore chose the PEDOT:PSS since it is a conductive film with a moderate conductivity in the THz range and an extremely thin profile [15]. Conversely, in a graphene-based FPC-LWA, a pair of electrodes is placed on top of the graphene sheet and on a conductive layer placed underneath of it. The conductive layer might be either a PEDOT:PSS [20], or a polysilicon layer [45]. In any case, it is important that the material between graphene and the conductive layer exhibits a high-voltage breakdown, so that graphene chemical potential can be raised at sufficiently high values to considerably change the conductive properties of the graphene sheet [20]. Examples of materials exhibiting a high-voltage breakdown are TiO_2 , Al_2O_3 , and HfO_2 [20]. As a final comment, we note that the thicknesses of the conductive layers and of the dielectric filling the gap with the graphene sheet are electrically small, and can therefore safely be neglected in the transmission line model of an FPC-LWA.

3. FPC-LWAs based on fishnet metasurfaces

3.1. Fishnet properties

A fishnet-like unit-cell can be obtained as a superposition of patches and strips of the same dimensions (see **Figure 3(a)**). Differently from array of patches and strip grating, this geometry

exhibits almost negligible spatial dispersion [15]. Therefore, the surface impedance of a fishnet-like unit-cell is accurately represented by a purely imaginary scalar impedance value $Z_s = jX_s$. As a matter of fact, this geometry has many other advantages with respect to the previous configurations [15]. As shown in [15], the fishnet design allows for spanning values of X_s from 100Ω to few ohms in the same parameter space. Thus, highly directive FPC-LWAs can be designed using a suitable combination of g and w values. In fact, since the fishnet element has a two-valued space parameter, the designer has more degrees of freedom to synthesize the required values of the impedance. For example, a reactance as low as $X_s = 15 \Omega$ can be synthesized by a fishnet unit-cell with $w = 0.4p$, $g = 0.2p$, and $p = \lambda_0/5 = 60 \mu m$, corresponding to $w = 24 \mu m$ and $g = 12 \mu m$, and thus fully compatible with a low-cost standard photolithographic fabrication process, as discussed in Section 2.6.

Therefore, the proposed fishnet element appears to be a valuable choice for the realization of the HMS since it allows for a flexible synthesis of the surface impedance. Moreover, its remarkably low spatial dispersion allows for a simple but accurate modeling, as will be shown in the next Section 3.2.

3.2. Fishnet-based design

The considered structure consists of a GDS made of Zeonor, covered with a fishnet-based HMS with parameters $g = 0.2p$ and $w = 0.4p$, in order to synthesize an impedance of 15Ω at 1 THz. While not spatially dispersive, the fishnet unit-cell is evidently frequency-dispersive, showing a quasi-linear frequency dependence [15], thus suggesting a dominant inductive behavior.

It is worth noting here that the negligible spatial dispersion of the fishnet allows for safely modeling the impedance $Z_s(f)$ as a function of the frequency f only, without including the dependence on the wavenumber (see [15] for further details). This model of $Z_s(f)$ has then been implemented in the equivalent circuit model depicted in **Figure 2** (replacing Z_{PRS} with $Z_s(f)$), to perform the dispersion analysis of the structure.

Numerical results are reported in **Figure 4(a)** where the behaviors of $\hat{\beta}_z$ (solid lines) and $\hat{\alpha}_z$ (dashed lines) are shown in the frequency range 0.5–1.5 THz for both TE (in red) and TM (in blue) polarizations. As expected, the fishnet acts as a very high reflective PRS (due to the low impedance value) and the resulting leaky modes are slight perturbations of those of an equivalent dielectric-filled PPW. The very low value of $\hat{\alpha}_z$ at the leaky cutoff $\beta_z \simeq \alpha_z$ suggests a very narrow pencil beam. This result is confirmed by the radiation patterns obtained through leaky-wave theory (black solid lines) and CST full-wave simulations (blue circles), as shown in **Figure 4(b)** for the E-plane and in **Figure 4(c)** for the H-plane. The remarkable agreement between the results confirms that the TE-TM leaky-wave pair is dominant, and that the radiation efficiency η_r is high.

In this regard, it is worth commenting on the overall expected efficiency e_r of this device to have a measure of the gain (G) rather than directivity (D_0) (we recall that $G = e_r D_0$). As a matter of fact, the very low but finite loss tangent of Zeonor [22] contributes to raise the leakage rate. Hence, we have determined the amount of leakage due to radiation $\hat{\alpha}_{rad}$, and that due to absorption $\hat{\alpha}_{loss}$ (where $\hat{\alpha}_z = \hat{\alpha}_{loss} + \hat{\alpha}_{rad}$) by running two different numerical

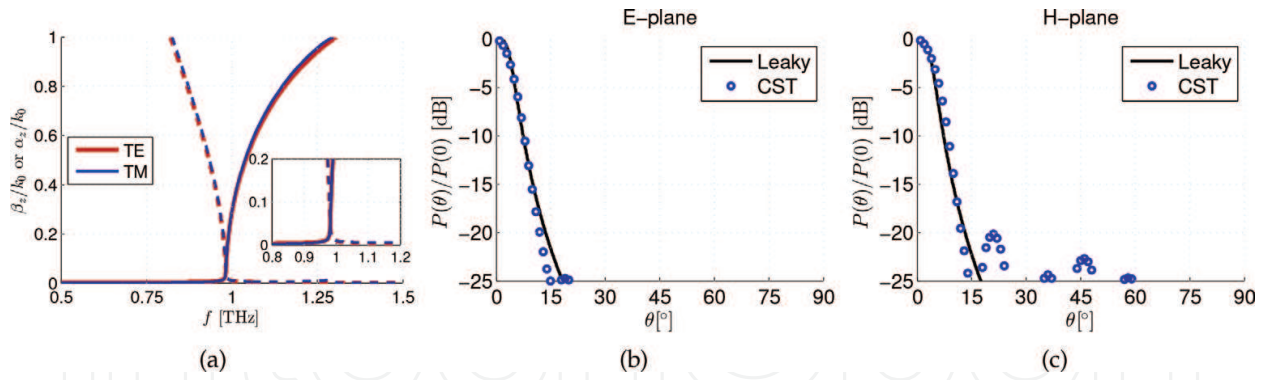


Figure 4 (a) Dispersion curves β_z/k_0 (solid lines) and α_z/k_0 vs. frequency (dashed lines) in the spectral range from 0.5 to 1.5 THz for TE (in red) and TM (in blue) polarizations. The inset highlights the behavior at the leaky cutoff, i.e., around $f = 1$ THz. (b) and (c) Normalized radiation patterns calculated with the leaky-wave approach (black solid lines) and validated with full-wave simulations (blue circles) are reported over the (b) E-plane and (c) H-plane [15].

simulations: one of the ideal, lossless structure to determine α_{rad} , and one of the lossy structures to determine α_z and in turn α_{loss} . With this method on hand, we obtained $e_r = 69\%$ for $L = 20\lambda_0$ (which leads to $\eta_r > 90\%$), and a gain greater than 26 dB.

4. FPC-LWAs based on graphene

4.1. Graphene properties

Graphene is a one-atom-thick layer of carbon atoms arranged in a honeycomb lattice with exceptional electronic transport properties [47]. From an antenna engineering point of view, one extremely interesting aspect of graphene theory is that due to its infinitesimal thickness, a graphene monolayer is adequately treated as a metasurface whose homogenized surface conductivity σ (neglecting nonlocal effects [51]) can be derived in scalar form by means of the Kubo formalism [47]. In the low THz range, i.e., for $0.3 \leq f \leq 3$ THz and at room temperature, i.e., $T = 300$ K, the complex-valued surface conductivity of graphene $\sigma = \sigma_R - j\sigma_I$ (where σ_R and $-\sigma_I$ expressed in Siemens [S] are the conductance and the susceptance of graphene equivalent admittance, respectively) is sufficiently well described by the following Drude-like expression [52, 53]:

$$\sigma = \sigma_R - j\sigma_I = \frac{2q_e^2 k_B T}{(\tau^{-1} + j\omega)\pi\hbar^2} \ln \left[2 \cosh \left(\frac{\mu_c}{2k_B T} \right) \right], \quad (10)$$

where $\omega = 2\pi f$ is the angular frequency, $-q_e$ is the electron charge, k_B is the Boltzmann constant, \hbar is the reduced Planck constant, τ is the *relaxation time* (which mainly determines graphene quality), and μ_c is the chemical potential. In the following, a relaxation time $\tau = 3$ ps is assumed.⁴

⁴Graphene quality strongly varies sample by sample, depending on several factors affecting the graphene synthesis. As a consequence, the relaxation time τ is never known *a priori*. The interested reader can refer to the recent detailed survey proposed in [49] as well as discussions in [20, 21].

Clearly, σ is strongly affected by the values of μ_c which in turn is related to the electrostatic bias E_0 through an integral equation [53]. As is known [20, 45, 53], the maximum absolute value of the chemical potential that can be obtained with an electrostatic field on the order of several V/nm (typically used in experiments⁵) is around 1 eV. It should be noted that such an electrostatic field is rather high and demands for the choice of suitable dielectric materials as discussed in Section 2.6.

Recent works [18, 20, 52, 53] have shown that in the THz range and for high-quality samples of graphene, the *resistive* part of graphene conductivity (σ_R) *slightly* increases as μ_c increases, whereas its *reactive* part (σ_I) *considerably* increases as μ_c increases. In particular, for high values of μ_c , σ becomes mostly reactive so that graphene can be switched from a bad to a good conductor when μ_c is raised in the range 0–1 eV. However, ohmic losses increase for high values of μ_c [20]. Hence, biased graphene, even if of good quality (high values of τ), behaves as a good conductor with nonnegligible ohmic losses in the considered THz range.

Nevertheless, the possibility to considerably change the surface conductivity through the application of a bias voltage is one of the most exceptional aspects of graphene behavior since it allows for designing FPC-LWAs with beam-steering capabilities at fixed frequency. Such devices will be the object of the next Section 4.2.

4.2. Graphene-based designs

In the simplest graphene-based FPC-LWA configuration, the PRS is replaced by a uniform (nonpatterned⁶) graphene sheet (see **Figure 5(a)**), possibly biased as discussed in Section 2.6. We call this configuration a graphene planar waveguide (GPW) [18]. As in a conventional FPC-LWA antenna design [12], the thickness of the dielectric layer h is set according to Eq. (4). Considering a GPW filled with a SiO₂ layer ($\epsilon_r = 3.8$) and operated at $f_0 = 1$ THz, it results $h \simeq 77 \mu\text{m}$. The GPW is therefore similar to the fishnet-based FPC-LWA seen in Section 3, but the presence of the graphene sheet in place of the fishnet allows for achieving beam scanning at a fixed frequency by tuning the graphene surface conductivity through the biasing scheme.

As shown in [18], if one solves the dispersion equations (see Eq. (6)) by replacing Y_{PRS} with σ^7 , one finds that the phase constants of the fundamental TE, TM leaky mode pair considerably change as the chemical potential μ_c is decreased from 1 to 0 eV. In particular, at $f = 0.922$ THz (corresponding to the leaky cutoff condition of the TM mode of a GPW biased at $\mu_c = 1$ eV [18]), the normalized phase constants of the leaky modes span values from about 0.2 to almost 1 for μ_c varying from 1 to 0 eV (see blue and red dashed lines in **Figure 6(a)** for the dispersion curves of the TM and the TE leaky modes of the GPW, respectively). According to Eq. (3), this allows for steering the beam from broadside to endfire.

⁵In recent experiments, bias voltages V_b on the order of 100 V have been applied across a grounded dielectric slab covered with a graphene sheet [54]. In that case, a slab of quartz ($\epsilon_r = 3.8$) of thickness $t = 300 \mu\text{m}$ was considered. Thus, for typical bias voltages in the range of 0 – 100 V, $E_0 = V_g/t$ would be in the range 0 – 1 V/nm [54].

⁶FPC-LWA designs based on patterned graphene sheets (namely, a 1-D array of capacitive strips of graphene) have been preliminarily investigated in [21].

⁷The same expression of σ can be used for both the TM and the TE polarization, since graphene exhibits negligible spatial dispersion, except for extremely slow waves such as surface plasmons [51], a case which is of no interest here.

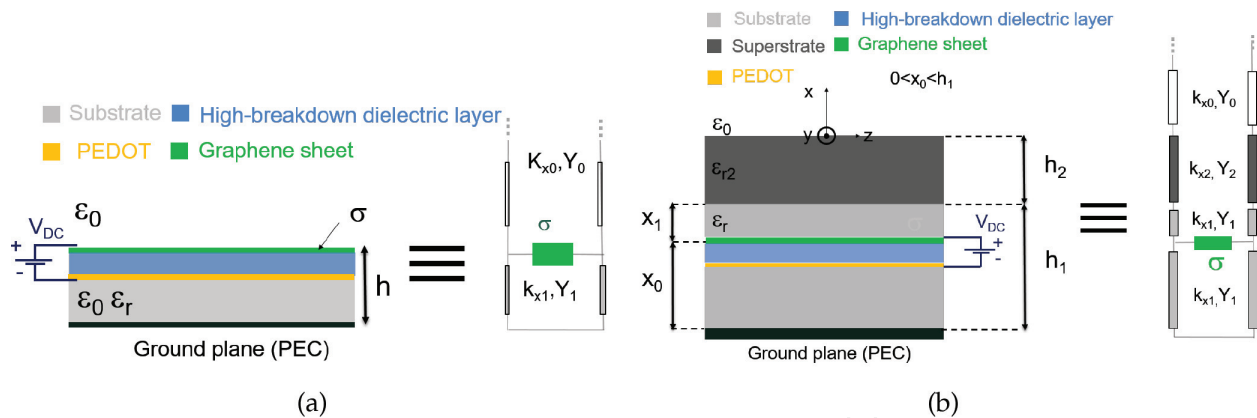


Figure 5. 2-D section and transmission line model of (a) a GPW and (b) a GSS [20].

The beam scanning capability through bias at fixed frequency is confirmed by the far-field radiation patterns (see colored dashed lines **Figures 6(b)** and **(c)**) obtained through CST full-wave simulations at $f = 0.922$ THz. As shown, for values of the chemical potential spanning from 1 to 0.5 eV, the GPW is able to steer the beam from broadside to 45° , respectively. However, the beamwidths are not very narrow (and, in turn, the directivities are rather low) due to the relatively large attenuation constant. This means that a graphene sheet alone is not sufficiently reflective as a PRS, even when highly biased.

To circumvent this issue, a slightly different configuration, also known as the graphene-based substrate-superstrate (GSS) antenna, has been proposed in the literature [19]. The idea underlying this novel configuration was the introduction of an additional *cover* layer on top of the GPW to increase the reflectivity of the overall PRS, now constituted by the combination of the graphene layer and the cover layer (see **Figure 5(b)**). Following the idea of a substrate-superstrate configuration, a quarter-wavelength dielectric material of high permittivity (namely, HfO_2 with $\epsilon_{r2} = 25$, thus fixing the thickness to $h_2 \approx 14 \mu\text{m}$) has been introduced on top of the GPW. However, the modal configuration of the tangential components of the electric field of an unperturbed substrate-superstrate structure (without the graphene sheet) has a minimum at the substrate-superstrate interface. As a consequence, a graphene sheet placed at the interface weakly interacts with the cavity and thus does not allow for achieving an effective reconfigurability of the pattern. This aspect poses the problem to find an optimal position for the graphene sheet within the cavity. As shown in [19], the position of the graphene sheet that maximizes the directivity in a GSS configuration is at $x_0 = 0.82h_1$ (see **Figure 5(b)**) for an operating frequency of $f = 1.132$ THz, i.e., in a middle way between a point of maximum interaction (i.e., the middle plane, $x_0 = 0.5h_1$) and a point of minimum interaction (i.e., the interface $x_0 = h_1$). The reason for this intermediate position is due to the nonnegligible ohmic losses of graphene, represented by the real part of its surface conductivity. Indeed, as the graphene sheet interacts more with the tangential electric field, the resonance effect increases (thus decreasing the leakage rate due to radiation $\hat{\alpha}_{\text{rad}}$), but also the contribution of the losses raises (thus increasing that part of the leakage rate accounting for the losses $\hat{\alpha}_{\text{loss}}$). As a result, the radiation efficiency and the directivity at broadside of a GSS strongly depend on the position of graphene inside the cavity. This has been quantitatively explained by the power analysis carried out in [20]. Unfortunately, the optimal position in terms of directivity at

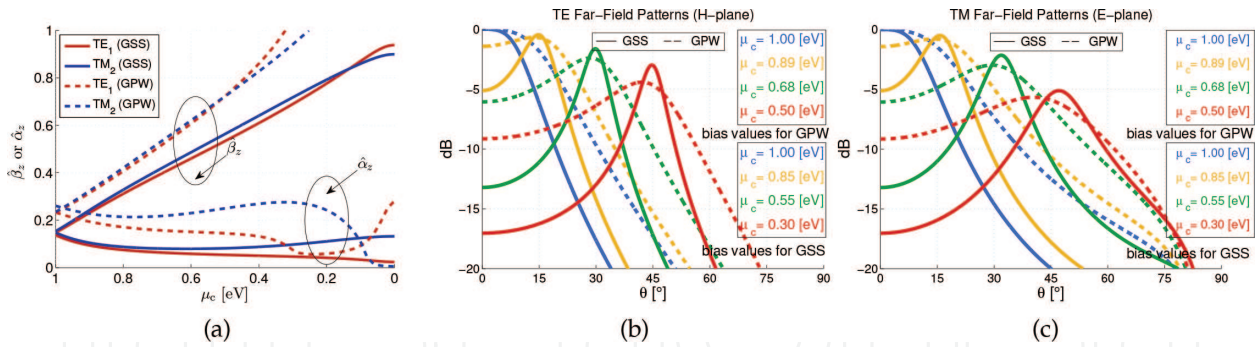


Figure 6 (a) Normalized phase constants and attenuation constants of the fundamental TM (in blue) and TE (in red) leaky modes of a GPW (dashed lines) at $f = 0.922$ THz and of a GSS (solid lines) with graphene placed at the optimum position $x_0 = 0.82h_1$ at a fixed frequency $f = 1.132$ THz, as a function of the chemical potential in the range $1 > \mu_c > 0$ eV. (b) H-plane and (c) E-plane radiation patterns, normalized to the overall maximum (achieved at broadside), vs. elevation angle θ for the GSS antenna (solid lines) and for the GPW (dashed lines). The scanning behavior at a fixed frequency ($f = 1.132$ THz for the GSS and $f = 0.92$ THz for the GPW) is shown for four theoretical pointing angles $\theta_0 = 0, 15, 30, 45^\circ$. The chemical potentials for the GPW and the GSS are reported in the legend [19].

broadside ($x_0 = 0.82h_1$) does not lead to the best configuration in terms of radiation efficiency ($x_0 = h_1$ or $x_0 = 0$). However, the radiation performance improvement in terms of directivity of a GSS with respect to a GPW is paid at the expense of a moderate reduction of radiation efficiency. To give some numbers, a GPW shows $D_0 \simeq 14$ dB and $e_r \simeq 69\%$, whereas an *optimized* GSS shows $D_0 \simeq 18.5$ dB and $e_r \simeq 56\%$.

The dispersion analysis of a GSS and its radiating performance are reported in **Figure 6(a)** (see blue and red solid lines for the dispersion curves of the TM and the TE leaky modes of the GPW, respectively) and **Figures 6(b)** and **(c)** (see colored solid lines). As manifested by comparing the dashed and solid colored lines in **Figures 6(b)** and **(c)**, the GSS shows considerably narrow beamwidths (thus higher directivities) over the entire beam scanning range. However, it should be noted that the GSS achieves the same angular range of a GPW over a wider range of variation of the chemical potential. This aspect reveals the slightly weaker degree of reconfigurability of the GSS with respect to the GPW.

5. FPC-LWAs based on nematic liquid crystals

5.1. NLC properties

Nematic liquid crystals (NLCs) are among the most widely studied and used liquid crystals (LCs). As is known [17], in addition to the solid crystalline and liquid phases, LCs exhibit intermediate phases (*mesophases*) where they flow like liquids (thus requiring hydrodynamical theories for their complete description), yet possess some physical properties characteristic of solids (thus requiring the *elastic continuum theory* for their complete description). As a function of temperature, or depending on the constituents, concentration, substituents, and so on, LCs exist in many so-called mesophases: *nematic*, *cholesteric*, *smectic*, and *ferroelectric* [17].

From an engineering point of view, LCs are attractive since, near the isotropic *nematic phase transition temperature*, the LC molecules become highly susceptible to external fields, and their responses tend to slow down considerably [17]. In particular, let us consider a layer of uniaxial

NLCs sandwiched between two substrates covered by electrodes. It is known that [17] if an alignment film is deposited on the substrates and no bias is applied ($V_b = 0$ V, *unbiased* state), the optical axis of the LC molecules is parallel to the substrate plane, in the direction given by the alignment film (horizontal axis), whereas, when a sufficiently large driving voltage ($V_b = V_\infty$, *biased* state) is applied across the LC, the optical axis is fully tilted and parallel to the applied electric field direction (vertical axis) [55]. While the maximum achievable tuning range can be inferred from the knowledge of these two limiting states, the voltage-dependent tunable properties of LCs require a rigorous study of the LC dynamics. This task can be performed by a numerical implementation of the Q-tensor theory of liquid crystals, a convenient theoretical formulation for the study of the LC orientation in confined geometries [56].

Among the different kinds of NLCs, we consider here the nematic mixture 1825 because of its high birefringence at THz frequencies [56]. The dielectric properties of such a material are described by a complex permittivity tensor $\underline{\underline{\epsilon}}_r$. As a uniaxial crystal, the permittivity tensor of an NLC in its unbiased and fully biased states reduces to a diagonal matrix, whose diagonal elements are the ordinary ϵ_o and extraordinary ϵ_e relative permittivities of the NLC. For intermediate states, the NLC permittivity tensor is no longer a diagonal matrix. However, a thorough analysis of the Q-tensor has revealed that for an NLC aligned along the horizontal z-axis (see the reference frame in **Figure 7**), when a low-driving voltage is applied [56] across a fishnet unit-cell, the optical axis of the NLC tilts in the xz -plane exhibiting a negligible rotation over both the yz - and the xy -plane. Thus, at first approximation⁸, the NLC can still be locally modeled as a *uniaxial* crystal whose complex permittivity tensor $\underline{\underline{\epsilon}}_r(V_b)$ is a diagonal matrix $\text{diag}(\epsilon_{xx}(V_b), \epsilon_{yy}, \epsilon_{zz}(V_b))$ where $\epsilon_{yy} = \epsilon_{xx}(0) = \epsilon_{zz}(V_\infty) = \epsilon_o \simeq 2.42$ and $\epsilon_{xx}(V_\infty) = \epsilon_{zz}(0) = \epsilon_e \simeq 3.76$ for a z-oriented NLC in the THz range [56], respectively. It is worth noting here that the assumption of uniaxial crystal for the NLC layer allows for easily describing its behavior with a relatively simple equivalent circuit model [57]. On the contrary, when the off-diagonal components are nonnegligible, more complicated equivalent networks are needed [57, 58], also accounting for the dielectric tensor spatial distribution [55].

5.2. NLC-based designs

The proposed device (see **Figure 7(a)**) consists of a multistack of alternating layers of thin alumina layers and of NLCs placed above a GDS. The choice of Zeonor for the substrate layer has been motivated by the index matching between its relative permittivity $\epsilon_{r1} = 2.3$ and the ordinary relative permittivity $\epsilon_o = 2.42$ of the NLC layer in the THz range [56], as it is required to properly enhance the resonance condition in an FPC [29].

As we have seen in Section 2.4, the alternation of high- and low-permittivity layers, with thicknesses fixed at odd multiples of a quarter wavelength in their respective media, allows for obtaining a narrow beam radiating at broadside [29]. In the proposed device, the innovating feature is represented by the possibility of exploiting the tunable properties of the NLCs [56], here representing the low-permittivity layer. In particular, the application of a common control signal to the NLC layers allows for changing their dielectric properties, thus achieving beam-steering capability at a fixed frequency, similar to the one obtained with the graphene-based FPC-LWAs shown in Section 4.

⁸ A more accurate model should take into account the non-zero values of the ϵ_{xz} and ϵ_{zx} components.

A circuit model (see **Figure 7(a)**) has been developed for the dispersion analysis of such a structure, taking into account the voltage dependence of the NLC layers. Hence, when no bias is applied ($V_b = 0$ V), the NLC molecules are aligned along the horizontal z -axis (**Figure 7(a)**), i.e., $\varepsilon_{zz}(0) = \varepsilon_e$, promoted by a few tens nm-thin alignment layer, which does not affect the electromagnetic properties of the device. When a sufficiently large driving voltage (V_∞) is applied across the LC layers, the NLC molecules reorient along the vertical x -axis, i.e., $\varepsilon_{zz}(V_\infty) = \varepsilon_o$, thus providing the maximum reconfigurability [55].

As a consequence, with reference to the transverse transmission line of **Figure 7(a)**, the characteristic admittances and the normal wavenumbers of the NLC layers for both the TE and the TM polarizations (with respect to the xz -plane) are functions of V_b . Their expressions are given by,

$$Y_0^{\text{TE}} = \hat{k}_x^{\text{TE}}/\eta_0, \quad \hat{k}_x^{\text{TE}} = \sqrt{\varepsilon_{yy} - \hat{k}_z^2}, \quad (11)$$

$$Y_0^{\text{TM}} = \left(\hat{k}_x^{\text{TM}} \eta_0\right)^{-1} \varepsilon_{zz}(V_b), \quad \hat{k}_x^{\text{TM}} = \sqrt{\frac{\varepsilon_{zz}(V_b)}{\varepsilon_{xx}(V_b)} \left(\varepsilon_{xx}(V_b) - \hat{k}_z^2\right)}, \quad (12)$$

Since ε_{yy} is the only component of the NLC which does not depend on V_b , only the TM leaky modes will be affected by the application of the bias; thus, the following discussion will be limited to the study of the fundamental TM leaky mode⁹. The dispersion equation of the TM modes is therefore computed as in Eq. (6), i.e., by replacing the Y_{PRS} with the input admittance seen looking upward the interface, and by modeling the characteristic admittances and the normal wavenumbers of each NLC transmission line segments with those given in Eq. (12).

In order to give a proof of concept, we have considered a layout with $N = 8$ layers (see [22] for this and other possible layouts), comprising three NLC cells and four alumina layers with thicknesses given by Eq. (9), assuming that $\varepsilon_r = \varepsilon_o$ as the thickness of the NLC cell. In this specific design, the choice of $f_0 = 0.59$ THz is dictated by the thickness of commercially available alumina thin layers ($127 \mu\text{m}$), which exhibit a relative permittivity $\varepsilon_{r2} = 9$ and a loss tangent of about $\tan \delta \simeq 0.01$ at 0.59 THz [22]¹⁰.

We have then evaluated the dispersion curves of the relevant TM leaky mode in the range 0.5 – 0.75 THz for different bias states. As shown in **Figure 7(b)**, the color of the curves gradually shades from yellow to blue when the bias V_b is changed from 0 (*unbiased* state) to a threshold voltage V_∞ (*biased* state), which can be accurately calculated through the method described in [22, 55]. For the proposed NLC cell, values below 20 V are sufficient to practically cover almost the whole switching range. In this simplified analysis, the relative permittivities are assumed to linearly vary with V_b . Thus, while the *unbiased* and *biased* states are always correctly predicted, the dynamic variation of $\hat{\beta}_z$ and $\hat{\alpha}_z$ for intermediate values of V_b could significantly change once the voltage dependence of $\underline{\underline{\varepsilon}}$ is computed.

⁹Note that the assumption of uniaxial crystal allows for decoupling the TM fields from the TE fields. This is not generally true when an anisotropic layer is at the interface with another medium, since in the most general case, more complicated networks are needed to describe its behavior [57, 58].

¹⁰We note here that, at $f = 0.59$ THz, the dielectric constant of Zeonor is the same, but the loss tangent is slightly higher, i.e., $\tan \delta \simeq 0.006$ [22].

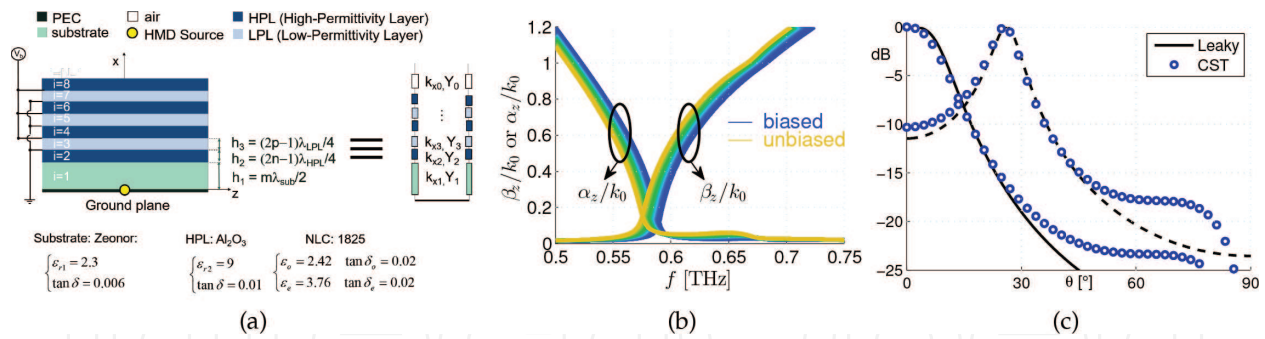


Figure 7. (a) 2-D cross section and transmission line model of the NLC-based FPC-LWA. (b) Dispersion curves ($\hat{\beta}_z$ and $\hat{\alpha}_z$ vs. f) of the fundamental TM leaky mode, when the NLC layer is biased at V_∞ (blue lines) and when it is unbiased at 0 V (yellow lines). Colors gradually shade from blue to yellow as V_b decreases from V_∞ to 0 V. (c) Radiation patterns considering the broadside operation (solid) and a scanned beam at the maximum pointing angle (dashed). The radiation patterns have been calculated by means of leaky-wave theory (black lines) and CST simulations (blue circles) for radiation at broadside and at the maximum pointing angle [22].

As expected, when $V_b = V_\infty$ (blue curve), the splitting condition $\hat{\beta}_z \approx \hat{\alpha}_z$ is achieved for $f = 0.59$ THz, which is the design frequency. Even more interestingly, once the frequency is fixed, e.g., at $f = 0.59$ THz, it is possible to change the value of the normalized phase constant $\hat{\beta}_z$, such that $\hat{\beta}_z > \hat{\alpha}_z$ by simply lowering the bias voltage, whereas the value of the normalized attenuation constant $\hat{\alpha}_z$ remains almost the same. As a consequence, the dispersion diagram of **Figure 7(b)** reveals the possibility to steer the beam with a quasi-constant beamwidth at a fixed frequency through bias voltage.

This is confirmed by the radiating patterns on the E-plane (the NLCs tunability affects only TM modes), calculated by means of leaky-wave theory (black lines) and CST full-wave simulations (blue circles), as shown in **Figure 7(c)**. Results have been reported in **Figure 7(c)** considering radiation at broadside (*biased* status) and at the maximum pointing angle (*unbiased* status). It should be noted that the radiation efficiency of this device is limited to values around 40% due to the nonnegligible losses introduced by the three NLC cells. However, if one reduces the number of NLC cells, the beam-steering capability of the device is reduced as well [22]. The interested reader can find a comparison of different FPC-LWAs based on NLCs in [22].

6. Conclusion

Fabry-Perot cavity leaky-wave antennas (FPC-LWAs) represent a valid solution for designing fully-planar, low-cost, high-gain antennas in the THz range. In this Chapter, starting from the conventional design of FPC-LWAs, the typical technological constraints of the submillimeter radiation have been thoroughly addressed to characterize the design criteria of THz FPC-LWAs. On this ground, three different THz-FPC LWA designs have been extensively discussed. First, an FPC-LWA based on a homogenized metasurface has been shown to produce high gain without requiring neither high complexity nor high fabrication cost. This has been made possible due to the employment of a fishnet unit-cell, a very interesting element for the impedance synthesis of metasurfaces in the THz range. This structure exhibits an excellent radiation performance, but it

does not offer pattern reconfigurability. To this purpose, two extremely interesting materials, namely graphene and nematic liquid crystals, have been employed for the design of two different reconfigurable THz FPC-LWAs. A closer look to the design and the radiation performance of these two novel reconfigurable THz FPC-LWAs has revealed that the reconfigurable properties of these classes of antennas are paid at the expense of a reduced radiation efficiency and an increase of the fabrication cost and complexity. However, THz technology is a continuously growing field, and the current technological constraints are expected to relax in the upcoming years, thus paving the way for the realization of new interesting reconfigurable and efficient THz FPC-LWAs as well.

Author details

Walter Fuscaldo^{1*}, Silvia Tofani¹, Paolo Burghignoli¹, Paolo Baccarelli² and Alessandro Galli¹

*Address all correspondence to: walter.fuscaldo@uniroma1.it

1 Department of Information Engineering, Electronics and Telecommunications, Sapienza University of Rome, Rome, Italy

2 Department of Engineering, Roma Tre University, Rome, Italy

References

- [1] Engheta N, Ziolkowski RW. *Metamaterials: Physics and Engineering Explorations*. Hoboken, NJ, USA: John Wiley & Sons; 2006
- [2] Williams WB, Pendry JB. Generating Bessel beams by use of localized modes. *Journal of the Optical Society of America. A*. 2005;**22**(5):992-997
- [3] Maci S, Minatti G, Casaletti M, Bosiljevac M. Metasurfing: Addressing waves on impenetrable metasurfaces. *IEEE Antennas and Wireless Propagation Letters*. 2011;**10**:1499-1502
- [4] Caloz C, Itoh T. *Electromagnetic Metamaterials: Transmission Line Theory and Microwave Applications*. Hoboken, NJ, USA: John Wiley & Sons; 2005
- [5] Siegel PH. Terahertz technology. *IEEE Transactions on Microwave Theory and Techniques*. 2002;**50**(3):910-928
- [6] Tonouchi M. Cutting-edge terahertz technology. *Nature Photonics*. 2007;**1**(2):97-105
- [7] Williams GP. Filling the THz gap—High power sources and applications. *Reports on Progress in Physics*. 2005;**69**(2):301
- [8] Lubecke VM, Mizuno K, Rebeiz GM. Micromachining for terahertz applications. *IEEE Transactions on Microwave Theory and Techniques*. 1998;**46**(11):1821-1831

- [9] Rebeiz GM. Millimeter-wave and terahertz integrated circuit antennas. *Proceedings of the IEEE*. 1992;**80**(11):1748-1770
- [10] Eleftheriades GV, Rebeiz GM. Design and analysis of quasi-integrated horn antennas for millimeter and submillimeter-wave applications. *IEEE Transactions on Microwave Theory and Techniques*. 1993;**41**(6):954-965
- [11] Chattopadhyay G, Reck T, Lee C, Jung-Kubiak C. Micromachined packaging for terahertz systems. *Proceedings of the IEEE*. 2017;**105**(6)
- [12] Jackson DR, Oliner AA. Leaky-wave antennas. In: Balanis CA, editor. *Modern Antenna Handbook*. New York, NY, USA: John Wiley & Sons; 2011 (ch. 7)
- [13] Llombart N, Chattopadhyay G, Skalare A, Mehdi I. Novel terahertz antenna based on a silicon lens fed by a leaky wave enhanced waveguide. *IEEE Transactions on Antennas and Propagation*. 2011;**59**(6):2160-2168
- [14] Neto A, Llombart N, Baselmans JJ, Baryshev A, Yates SJ. Demonstration of the leaky lens antenna at submillimeter wavelengths. *IEEE Transactions on Terahertz Science and Technology*. 2014;**4**(1):26-32
- [15] Fuscaldo W, Tofani S, Zografopoulos DC, Baccarelli P, Burghignoli P, Beccherelli R, Galli A. Systematic design of THz leaky-wave antennas based on homogenized metasurfaces. *IEEE Transactions on Antennas and Propagation*. 2018;**66**(3):1169-1178
- [16] Neto AHC, Guinea F, Peres NM, Novoselov KS, Geim AK. The electronic properties of graphene. *Reviews of Modern Physics*. 2009;**81**(1):109
- [17] Khoo I-C. *Liquid Crystals: Physical Properties and Nonlinear Optical Phenomena*. Vol. 64. Hoboken, NJ, USA: John Wiley & Sons; 2007
- [18] Fuscaldo W, Burghignoli P, Baccarelli P, Galli A. Complex mode spectra of graphene-based planar structures for THz applications. *Journal of Infrared, Millimeter, and Terahertz Waves*. 2015;**36**(8):720-733
- [19] Fuscaldo W, Burghignoli P, Baccarelli P, Galli A. A reconfigurable substrate-superstrate graphene-based leaky-wave THz antenna. *IEEE Antennas and Wireless Propagation Letters*. 2016;**15**:1545-1548
- [20] Fuscaldo W, Burghignoli P, Baccarelli P, Galli A. Graphene Fabry-Perot cavity leaky-wave antennas: Plasmonic versus nonplasmonic solutions. *IEEE Transactions on Antennas and Propagation*. 2017;**65**(4):1651-1660
- [21] Fuscaldo W, Burghignoli P, Baccarelli P, Galli A. Efficient 2-D leaky-wave antenna configurations based on graphene metasurfaces. *International Journal of Microwave and Wireless Technologies*. 2017;**9**(6):1293-1303
- [22] Fuscaldo W, Tofani S, Zografopoulos DC, Baccarelli P, Burghignoli P, Beccherelli R, Galli A. Tunable Fabry-Perot cavity THz antenna based on leaky-wave propagation in nematic liquid crystals. *IEEE Antennas and Wireless Propagation Letters*. 2017;**16**:2046-2049

- [23] Ip A, Jackson DR. Radiation from cylindrical leaky waves. *IEEE Transactions on Antennas and Propagation*. 1990;**38**(4):482-488
- [24] Zhao T, Jackson DR, Williams JT, Oliner AA. General formulas for 2-D leaky-wave antennas. *IEEE Transactions on Antennas and Propagation*. 2005;**53**(11):3525-3533
- [25] Von Trentini G. Partially reflecting sheet arrays. *IRE Transactions on Antennas and Propagation*. 1956;**4**(4):666-671
- [26] Lovat G, Burghignoli P, Jackson DR. Fundamental properties and optimization of broad-side radiation from uniform leaky-wave antennas. *IEEE Transactions on Antennas and Propagation*. 2006;**54**(5):1442-1452
- [27] Jackson DR, Alexópoulos NG. Gain enhancement methods for printed circuit antennas. *IEEE Transactions on Antennas and Propagation*. 1985;**33**:976-987
- [28] Jackson DR, Oliner AA. A leaky-wave analysis of the high-gain printed antenna configuration. *IEEE Transactions on Antennas and Propagation*. 1988;**36**(7):905-910
- [29] Jackson DR, Oliner AA, Ip A. Leaky-wave propagation and radiation for a narrow-beam multiple-layer dielectric structure. *IEEE Transactions on Antennas and Propagation*. 1993;**41**(3):344-348
- [30] Tamir T, Oliner AA. Guided complex waves. Part 1: Fields at an interface. *Proceedings of the IEE*. 1963;**110**(2):310-324
- [31] Tamir T, Oliner AA. Guided complex waves. Part 2: Relation to radiation patterns. *Proceedings of the IEE*. 1963;**110**(2):325-334
- [32] Baccarelli P, Burghignoli P, Frezza F, Galli A, Lampariello P, Lovat G, Paulotto S. Effects of leaky-wave propagation in metamaterial grounded slabs excited by a dipole source. *IEEE Transactions on Microwave Theory and Techniques*. 2005;**53**(1):32-44
- [33] Di Nallo C, Frezza F, Galli A, Lampariello P. Rigorous evaluation of ohmic-loss effects for accurate design of traveling-wave antennas. *Journal of Electromagnetic Waves and Applications*. 1998;**12**(1):39-58
- [34] Luukkonen O, Simovski C, Granet G, Goussetis G, Lioubtchenko D, et al. Simple and accurate analytical model of planar grids and high-impedance surfaces comprising metal strips or patches. *IEEE Transactions on Antennas and Propagation*. 2008;**56**(6):1624-1632
- [35] Holloway CL, Dienstfrey A, Kuester EF, O'Hara JF, Azad AK, Taylor AJ. A discussion on the interpretation and characterization of metafilms/metasurfaces: The two-dimensional equivalent of metamaterials. *Metamaterials*. 2009;**3**(2):100-112
- [36] Fuscaldo W, Jackson DR, Galli A. A general and accurate formula for the beamwidth of 1-D leaky-wave antennas. *IEEE Transactions on Antennas and Propagation*. 2017;**65**(4):1670-1679

- [37] Fuscaldo W, Jackson DR, Galli A. Beamwidth properties of endfire 1-D leaky-wave antennas. *IEEE Transactions on Antennas and Propagation*. 2017;**65**(11):6120-6125
- [38] Pozar DM. *Microwave Engineering*. Hoboken, NJ, USA: John Wiley & Sons; 2009
- [39] Gordon JA, Holloway CL, Dienstfrey A. A physical explanation of angle-independent reflection and transmission properties of metafilms/metasurfaces. *IEEE Antennas and Wireless Propagation Letters*. 2009;**8**:1127-1130
- [40] Alexópoulos NG, Jackson DR. Fundamental superstrate (cover) effects on printed circuit antennas. *IEEE Transactions on Antennas and Propagation*. 1984;**32**(8):807-816
- [41] Yang H, Alexópoulos NG. Gain enhancement methods for printed circuit antennas through multiple superstrates. *IEEE Transactions on Antennas and Propagation*. 1987;**35**(7):860-863
- [42] Thevenot M, Cheype C, Reineix A, Jecko B. Directive photonic-bandgap antennas. *IEEE Transactions on Microwave Theory and Techniques*. 1999;**47**(11):2115-2122
- [43] Ji L-Y, Guo YJ, Qin P-Y, Gong S-X, Mittra R. A reconfigurable partially reflective surface (PRS) antenna for beam steering. *IEEE Transactions on Antennas and Propagation*. 2015;**63**(6):2387-2395
- [44] Lovat G, Burghignoli P, Celozzi S. A tunable ferroelectric antenna for fixed-frequency scanning applications. *IEEE Antennas and Wireless Propagation Letters*. 2006;**5**(1):353-356
- [45] Esquiús-Morote M, Gómez-Daz JS, Perruisseau-Carrier J. Sinusoidally modulated graphene leaky-wave antenna for electronic beamscanning at THz. *IEEE Transactions on Terahertz Science and Technology*. 2014;**4**(1):116-122
- [46] Wang X-C, Zhao W-S, Hu J, Yin W-Y. Reconfigurable terahertz leaky-wave antenna using graphene-based high-impedance surface. *IEEE Transactions on Nanotechnology*. 2015;**14**(1):62-69
- [47] Geim AK, Novoselov KS. The rise of graphene. *Nature Materials*. 2007;**6**(3):183-191
- [48] Konar A, Fang T, Jena D. Effect of high- k gate dielectrics on charge transport in graphene-based field effect transistors. *Physical Review B*. 2010;**82**(11):115452
- [49] Zouaghi W, Voß D, Gorath M, Nicoloso N, Roskos HG. How good would the conductivity of graphene have to be to make single-layer-graphene metamaterials for terahertz frequencies feasible? *Carbon*. 2015;**94**:301-308
- [50] Lo YH, Leonhardt R. Aspheric lenses for terahertz imaging. *Optics Express*. 2008;**16**(20):15991-15998
- [51] Lovat G, Hanson GW, Araneo R, Burghignoli P. Semiclassical spatially dispersive intra-band conductivity tensor and quantum capacitance of graphene. *Physical Review B*. 2013;**87**(11):115429

- [52] Hanson GW. Dyadic Green's functions and guided surface waves for a surface conductivity model of graphene. *Journal of Applied Physics*. 2008;**103**(6):064302
- [53] Hanson GW. Dyadic Green's functions for an anisotropic, non-local model of biased graphene. *IEEE Transactions on Antennas and Propagation*. 2008;**56**(3):747-757
- [54] Novoselov KS, Geim AK, Morozov SV, Jiang D, Katsnelson MI, Grigorieva IV, Dubonos SV, Firsov AA. Two-dimensional gas of massless Dirac fermions in graphene. *Nature*. 2005; **438**(7065):197-200
- [55] Bellini B, Beccherelli R. Modelling, design and analysis of liquid crystal waveguides in preferentially etched silicon grooves. *The Journal of Physics D: Applied Physics*. 2009;**42**(4): 045111
- [56] Zografopoulos DC, Beccherelli R. Tunable terahertz fishnet metamaterials based on thin nematic liquid crystal layers for fast switching. *Scientific Reports*. 2015;**5**(13137):1-11
- [57] Collin RE. *Field Theory of Guided Waves*. New York, NY, USA: McGraw-Hill; 1991
- [58] Pavone SC, Martini E, Caminita F, Albani M, Maci S. Surface wave dispersion for a tunable grounded liquid crystal substrate without and with metasurface on top. *IEEE Transactions on Antennas and Propagation*. 2017;**65**(7):3540-3548